ACS NANO
Cite This: ACS Nano 2019, 13, 11741−11752
www.acsnano.org

ARTICLE

Direct Imaging of Interfacial Fluctuations in Confined Block Copolymer with *in Situ* Slow-Scan-Disabled Atomic Force Microscopy

Jonathan G. Raybin,[†] Julia G. Murphy,[†] Moshe Dolejsi,[‡] and S. J. Sibener*[,†]

[†]The James Franck Institute and Department of Chemistry, The University of Chicago, 929 E. 57th Street, Chicago, Illinois 60637, United States

[‡]The Pritzker School for Molecular Engineering, The University of Chicago, 5640 S. Ellis Avenue, Chicago, Illinois 60637, United States

Supporting Information

ABSTRACT: **Using environmentally controlled, high-speed atomic force microscopy (AFM), we examine dynamic fluctuations of topographically confined poly(styrene-*block*-methyl methacrylate) (PS-*b*-PMMA) cylinders. During thermal annealing, fluctuations drive perturbations of the block copolymer (BCP) interface between polymer domains, leading to pattern roughness. Whereas previous investigations have examined roughness in room-temperature and kinetically quenched samples, we directly visualize the dynamics of PS/PMMA interfaces in real space and time at *in situ* temperatures above the glass transition temperature, T_g. Imaging under these experimentally challenging thermal annealing conditions is critical to understanding the inherent connection between thermal fluctuations and BCP pattern assembly. Through the use of slow-scan-disabled AFM, we dramatically improve the imaging time resolution for tracking polymer dynamics. Fluctuations increase in intensity with temperature and, at high temperatures, become spatially coherent across their confining potential. Additionally, we observe that topographic confinement suppresses fluctuations and correlations in the proximity of the guiding field. *In situ* imaging at annealing temperatures represents a significant step in capturing the dynamics of chain mobility at BCP interfaces.**

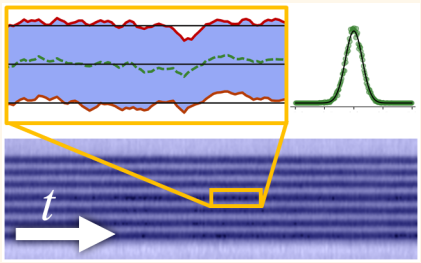

KEYWORDS: *atomic force microscopy, block copolymer, directed self-assembly, fluctuations, graphoepitaxy, line roughness, poly(styrene-block-methyl methacrylate)*

The length scale and regularity of self-assembled block copolymer (BCP) patterns make them attractive candidates for next-generation lithographic and templating applications.[1,2] BCP films natively self-assemble to form periodic nanostructures, including spherical, cylindrical, gyroid, and lamellar phases.[3,4] This self-assembly process is thermodynamically driven by microphase separation of the polymer domains as governed by χ, the Flory−Huggins interaction parameter between polymer segments. Strongly segregated BCPs produce well-defined features that may be transferred onto hard substrates for subsequent lithographic processing. While the dimensions of BCP domains are favorable for device applications, in the absence of an external guiding field, the patterns lack long-range order and form a randomly oriented fingerprint-like pattern. Traditional top-down lithography can be used to engineer the polymer substrate, through processes known as directed self-assembly (DSA), to create local fields for controlling domain orientation and alignment. Chemical[5,6] or topographic[7−9] templates induce the organization of globally ordered BCP nanostructures, advantageous for both device fabrication and for creating stable environments to study BCP assembly. In particular, graphoepitaxial control using topographically patterned substrates enforces the alignment of confined polymer cylinders using the trench sidewalls as well-defined boundary conditions.

DSA-templated systems have been extensively studied with a focus on producing long-range domain alignment[10−12] and removing point defects.[13−15] Concerted effort by the DSA community has resulted in the realization of single-crystal, essentially defect-free BCP thin films on the 300 mm wafer scale.[12,16] Nevertheless, even with perfect domain connectivity and control over defect density, structural disorder remains in BCP thin films.[17−19] Pattern roughness, which arises from bulk composition fluctuations in segregated polymer domains,[20−22] is enhanced by thermally excited interfacial dynamics.[23,24] A deeper understanding of these boundary dynamics is essential

Received: July 21, 2019
Accepted: October 4, 2019
Published: October 11, 2019

DOI: 10.1021/acsnano.9b05720
ACS Nano 2019, 13, 11741−11752

to understanding the intrinsic role of fluctuations in defect healing and driving changes in pattern connectivity.

Researchers have developed a variety of models and experimental methods to fully characterize line roughness, including its spatial correlation and spectral dependence.[25−28] Stein *et al.* compared the use of soft X-ray diffraction and scanning electron microscopy as tools for nondestructively measuring domain roughness, which they modeled as interfacial capillary waves.[24] Further investigation by Bosse employed computer-simulated phase-field models to track the effects of temperature, segregation strength, and confinement on roughness.[29−31] In his theoretical treatment of confined BCP ordering, Bosse demonstrated that the line-edge roughness (LER) power spectra of lamellae-forming BCP can be modeled with a two-term expression that includes the contributions of thermal capillary wave fluctuations and bulk composition fluctuations.[31] Ruiz *et al.* adapted Bosse's model by modifying the description of interfacial dynamics to include a set of undulatory and peristaltic modes.[32] These modes correspond to line-placement roughness (LPR) and line-width roughness (LWR), respectively, following a phenomenological description used for bilayer membranes. Additionally, while traditional imaging techniques are limited to the polymer surface, several experiments have investigated interfacial fluctuations in three dimensions—through modeling of the reciprocal space signal with X-ray diffraction[33,34] and in real space with transmission electron microscope tomography[35]—to develop a complete, through-film description of roughness and to characterize the effects of substrate interactions.

The previously described experimental studies examined roughness in systems cooled below the glass transition T_g, that is, at temperatures where dynamic fluctuations are quenched. While low-temperature analysis can quantify residual spatial roughness, these methods are limited to static systems and cannot separate the effect of fluctuation damping during the cooling process. Measurements above T_g are essential for directly visualizing the dynamics of BCP patterns, which, alongside domain fluctuations, include defect healing[13,36,37] and domain alignment.[10,38] Using *in situ* AFM heating techniques, several groups have independently investigated the behavior of BCP interfaces during thermal annealing. Tsarkova *et al.* observed periodic undulations of domain boundaries and found qualitative correlations between the fluctuations of adjacent domains.[39,40] When studying the formation and growth of BCP microdomains, Yufa *et al.* measured spatiotemporal autocorrelation of the interdomain boundary structure and observed an interfacial restoring force resulting from curvature minimization.[41]

Recent advancements in high-speed AFM have significantly improved instrumental stability and imaging rates, enhancing our ability to track domain fluctuations.[42] Together, these developments allow us to achieve sufficient fidelity to characterize interfacial dynamics during the thermal annealing process. In this work, we apply *in situ* AFM imaging to measure fluctuations in topographically confined cylinder-forming poly(styrene-*block*-methyl methacrylate) (PS-*b*-PMMA). Although lamellae are more widely used in lithographic applications, a cylinder-forming BCP was selected as a model system for mapping interfacial fluctuations due to the relative simplicity of preparation under confinement.[2] The aligned BCP cylinders act as a controlled environment for analyzing disorder under varying experimental conditions, including temperature and confinement strength. Because of the asymmetric volume fraction in cylinder morphologies, the minority block exhibits enhanced coherence within the majority matrix. In this report, we describe the use of slow-scan-disabled AFM imaging to directly capture and quantify the interdomain fluctuations in confined BCP and show that these fluctuations increase in intensity and become spatially coherent with temperature. Ultimately, this method provides direct experimental insight of BCP fluctuations in real time and real space, illuminating their contribution to interfacial roughness, defect healing,[39] and pattern aging.[43,44]

RESULTS AND DISCUSSION

SSD Imaging. To optimize our time resolution, images are acquired in the slow-scan-disabled (SSD) AFM mode. An example SSD AFM image is shown in Figure 1, in which the slow-scan axis is disabled midway through the AFM scan, as indicated by the white horizontal line. The AFM phase image shows aligned PS-*b*-PMMA cylinders within a topographic trench flanked by two neighboring regions of unconfined fingerprint pattern; the PS and PMMA domains appear as light and dark blue, respectively. Above the dividing line, Figure 1 shows a conventional AFM image, as collected over a two-dimensional surface raster. Then, after the slow-scan axis is disabled, the AFM probe begins to continuously trace over the same line of the sample along the *x*-axis, enabling rapid sampling of a single one-dimensional cross-section of the surface. With this technique, the *y*-axis of the image becomes time, while, as usual, the *x*-axis indicates the lateral position of the probe. With typical high-speed AFM imaging under our experimental conditions, a full image with 512 lines takes 25 s. By disabling the slow-scan axis, the effective time resolution is enhanced to 50 ms, while still fully capturing the dynamics of a single cross-section.

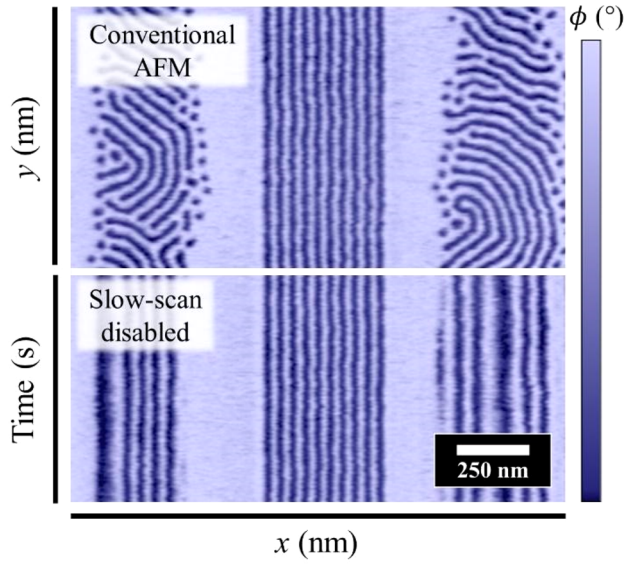

Figure 1. AFM phase channel image of aligned PS-*b*-PMMA cylinders within a topographic trench, with surrounding regions of unconfined fingerprint pattern; the PS and PMMA domains are light and dark blue, respectively. The slow-scan axis is disabled midway through the scan, as indicated by the white horizontal line, and the *y*-axis becomes time while the *x*-axis remains the lateral position. Disabling the slow-scan axis increases the effective sampling time resolution to 50 ms.

DOI: 10.1021/acsnano.9b05720
ACS Nano 2019, 13, 11741−11752

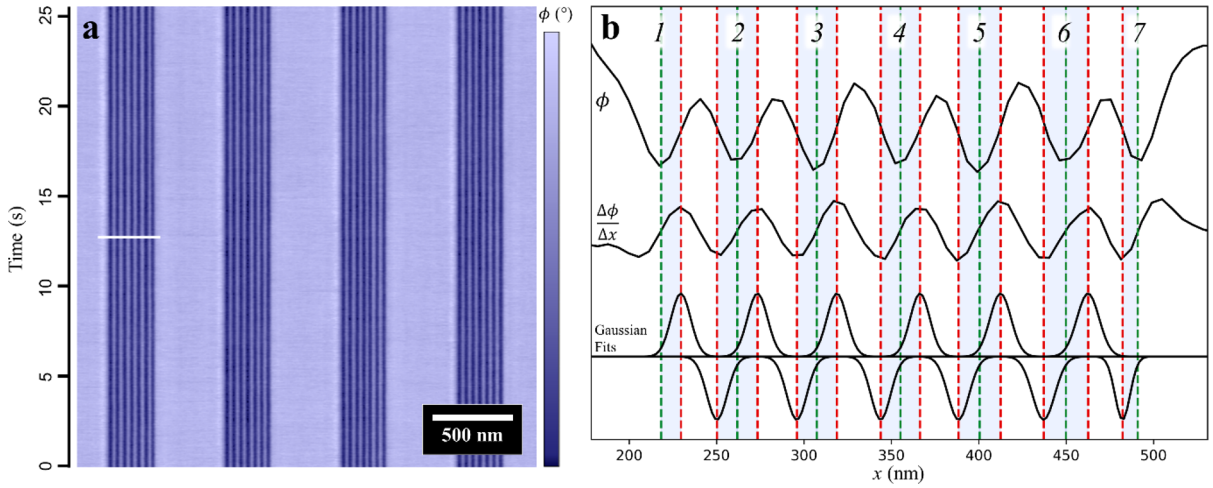

Figure 2. (a) SSD AFM phase channel image of aligned PS-*b*-PMMA cylinders in a confining trench. Phase contrast distinguishes PS (light blue) and PMMA (dark blue). Because the slow-scan axis is disabled, the *y*-axis of the image measures time. A phase ϕ cross-section of the seven cylinders, marked as a white horizontal line across the first trench, is plotted in (b). The $\Delta\phi/\Delta x$ derivative curve and associated Gaussian fits are used to determine the position of cylinder edges (dashed red lines), placements (dashed green lines), and widths (blue shaded areas). The left- and rightmost interfaces are not fit, as maxima are poorly defined at the trench sidewalls.

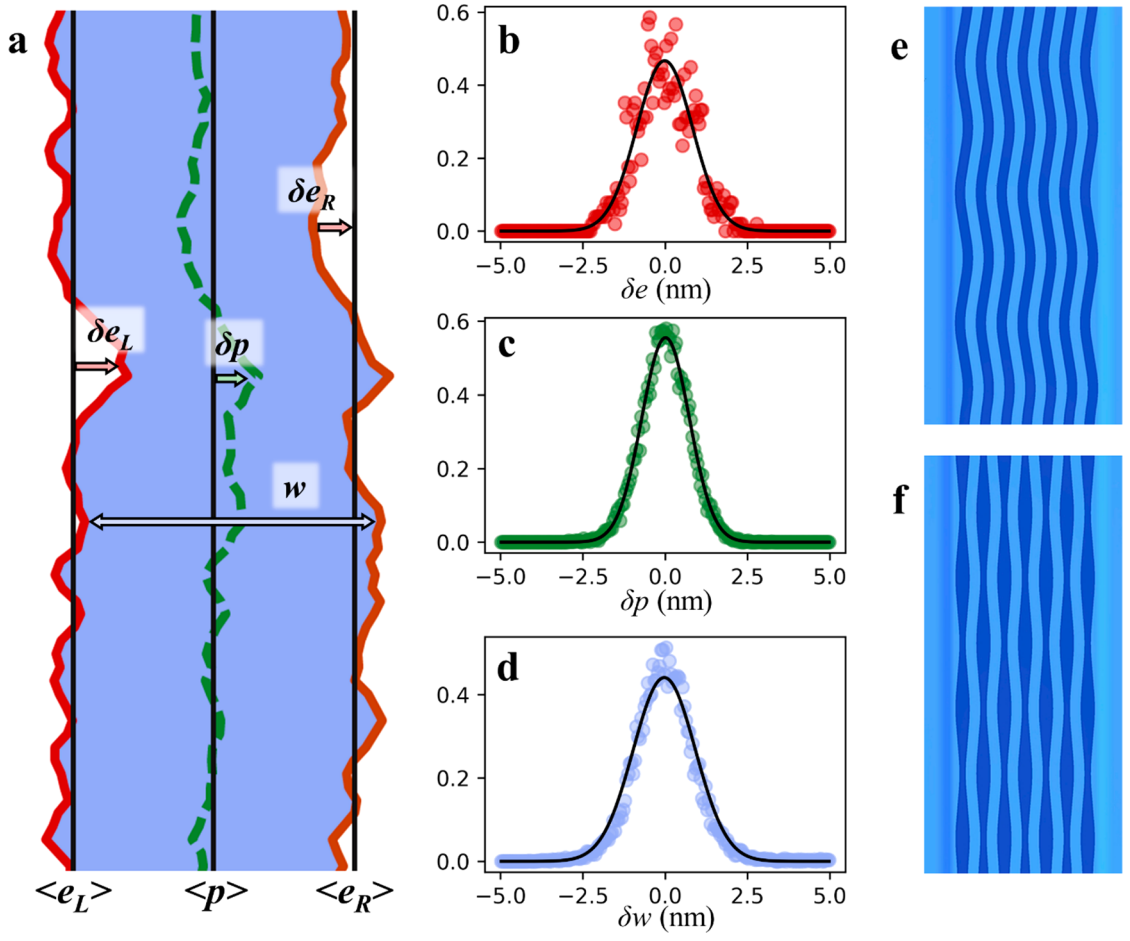

Figure 3. (a) Schematic including definitions for cylinders edges, $\langle e \rangle$, placements, $\langle p \rangle$, and widths, $\langle w \rangle$ averaged over time and their residuals δe, δp, and δw. (b–d) Measurements at 150 °C of the respective residuals (red, green, and blue points) for each of these parameters, follow Gaussian distributions (black fit lines). Cylinder fluctuations include contributions from (e) correlated edge fluctuations and (f) anticorrelated edge fluctuations.

As an example of our method, an SSD image of aligned polymer cylinders in four lithographic trenches is shown in Figure 2a. The PS and PMMA domains have strong contrast in the phase due to differences in energy dissipation at the AFM tip, allowing us to distinguish between the two blocks.[37] Peaks and valleys in ϕ, shown in Figure 2b, correspond to the PS

DOI: 10.1021/acsnano.9b05720
ACS Nano 2019, 13, 11741−11752

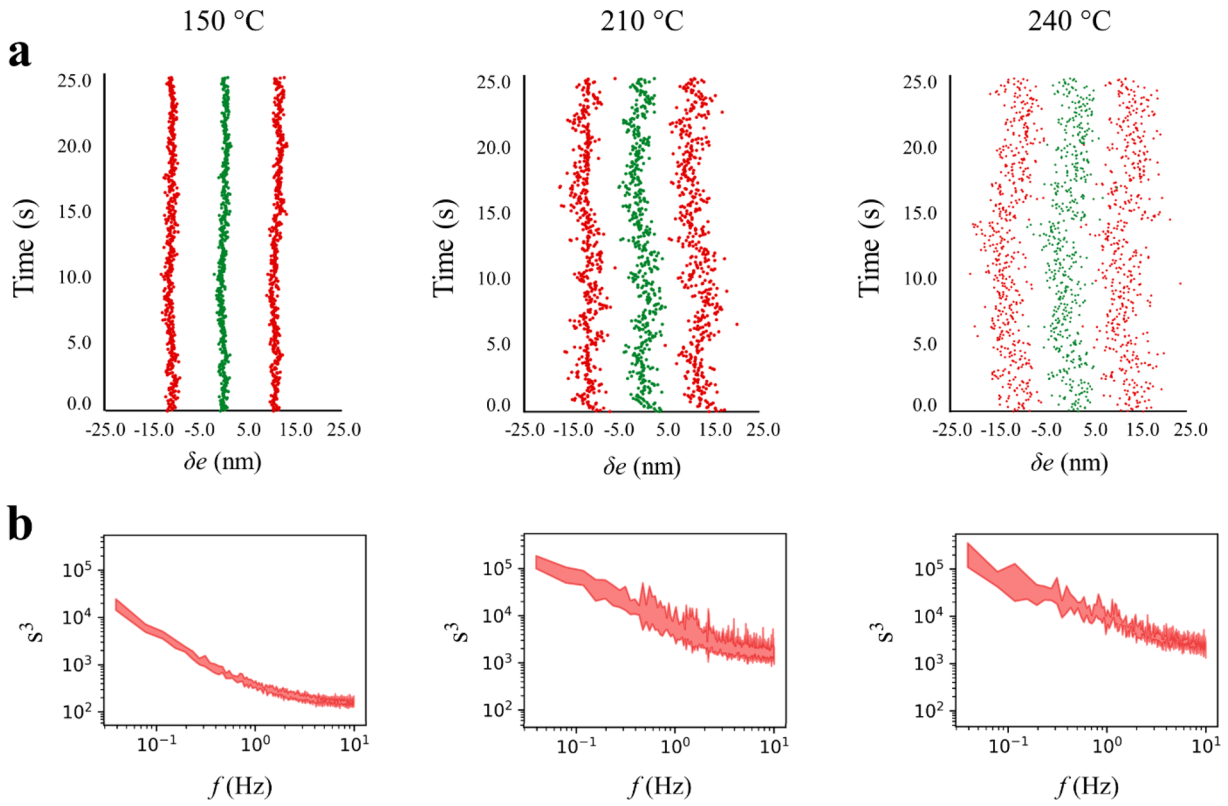

Figure 4. (a) Representative trajectories showing edge (red points) and placement (green points) residuals of a PMMA cylinder at 150, 210, and 240 °C. Trajectories show strong spatial correlation, but have insufficient time resolution to fully capture polymer dynamics. (b) Corresponding discrete PSD plots of the spectral roughness as a function of temporal frequency at each temperature. The red bands indicate the first standard deviation bounds of the discrete PSD as averaged over cylinder trajectories in 3−10 AFM images. Roughness spectra increase in magnitude and flatten with increasing temperature.

matrix and PMMA cylinders, respectively, in the image cross-section, marked as a line scan in Figure 2a. We identify the domain interfaces as the points of greatest change in phase, determined from the extrema of the first-derivative signal $\Delta\phi/\Delta x$. BCP domain interfaces are often described as arctangents or error functions.[21,45] We therefore model the boundary line using a Gaussian fit to the first derivative signal. Further details on Gaussian fitting are included in Figure S1 in the Supporting Information. Each guiding trench contains seven PMMA cylinders, indexed $i = 1-7$, and each has two corresponding domain interfaces, with positions $e_{i,n}$, where $n = L$ or R denote the left and right edges. We obtain the cylinder placement p_i from the average of the left and right edge positions and the width w_i from the edge separation:

$$p_i = 1/2(e_{i,L} + e_{i,R}); \quad w_i = (e_{i,R} - e_{i,L}) \tag{1}$$

In our confined system, cylinders have a confined pitch of 46.5 ± 4.1 nm, which remains stable over the temperatures surveyed, as shown in Supporting Information, Figure S2. This pitch slightly exceeds the native cylinder periodicity L_0 of our BCP, 44.1 ± 1.7 nm, as measured in thin-film samples without lateral confinement. The polymer pattern is moderately incommensurate with the trench width, and the resulting strain is distributed between the cylinder domains.[8] Our measurements examine fluctuations of these domains within the free energy landscape defined by the confining trenches.

Within the trenches, the film topography varies slowly with respect to the AFM tip radius, and phase imaging serves as a true measure of the surface composition. However, along the boundaries of the trench, where the film height changes rapidly, we see an unavoidable convolution of the phase signal due to coupling with the sample topography. Interactions between the AFM probe and the trench sidewall dissipate energy, leading to a change in the phase offset.[46] As a result, we cannot directly identify the position of the left- and rightmost cylinder edges, that is, $e_{1,L}$ and $e_{7,R}$, from the first-derivative signal. Instead we assign the location of these edges by assuming the cylinders are symmetric about their central position, determined from the ϕ minima for these cylinders. Because of this methodological discrepancy, these edges are omitted from analysis of spatial correlations.

Time-Dependent Trajectories. Our *in situ* imaging directly captures the time-dependent fluctuations of each domain boundary. Each SSD image includes 512 linescan traces, which together produce a time-resolved trajectory of the fluctuations for each PS/PMMA interface $e_{i,n}(t)$. The position of the i-th interface fluctuates from its average point, with residual:

$$\delta e_{i,n}(t) = e_{i,n}(t) - \langle e_{i,n} \rangle \tag{2}$$

where $\langle \cdot \rangle$ represents the time average. These terms are illustrated in the schematic in Figure 3a. From the edge trajectories, we obtain the corresponding placement $p_i(t)$ and width $w_i(t)$ time series for each cylinder, with residuals:

$$\delta p_i(t) = p_i(t) - \langle p_i \rangle; \quad \delta w_i(t) = w_i(t) - \langle w_i \rangle \tag{3}$$

The fluctuations for each term are observed to be normally distributed about their equilibrium values, as shown in Figure

DOI: 10.1021/acsnano.9b05720
ACS Nano 2019, 13, 11741−11752

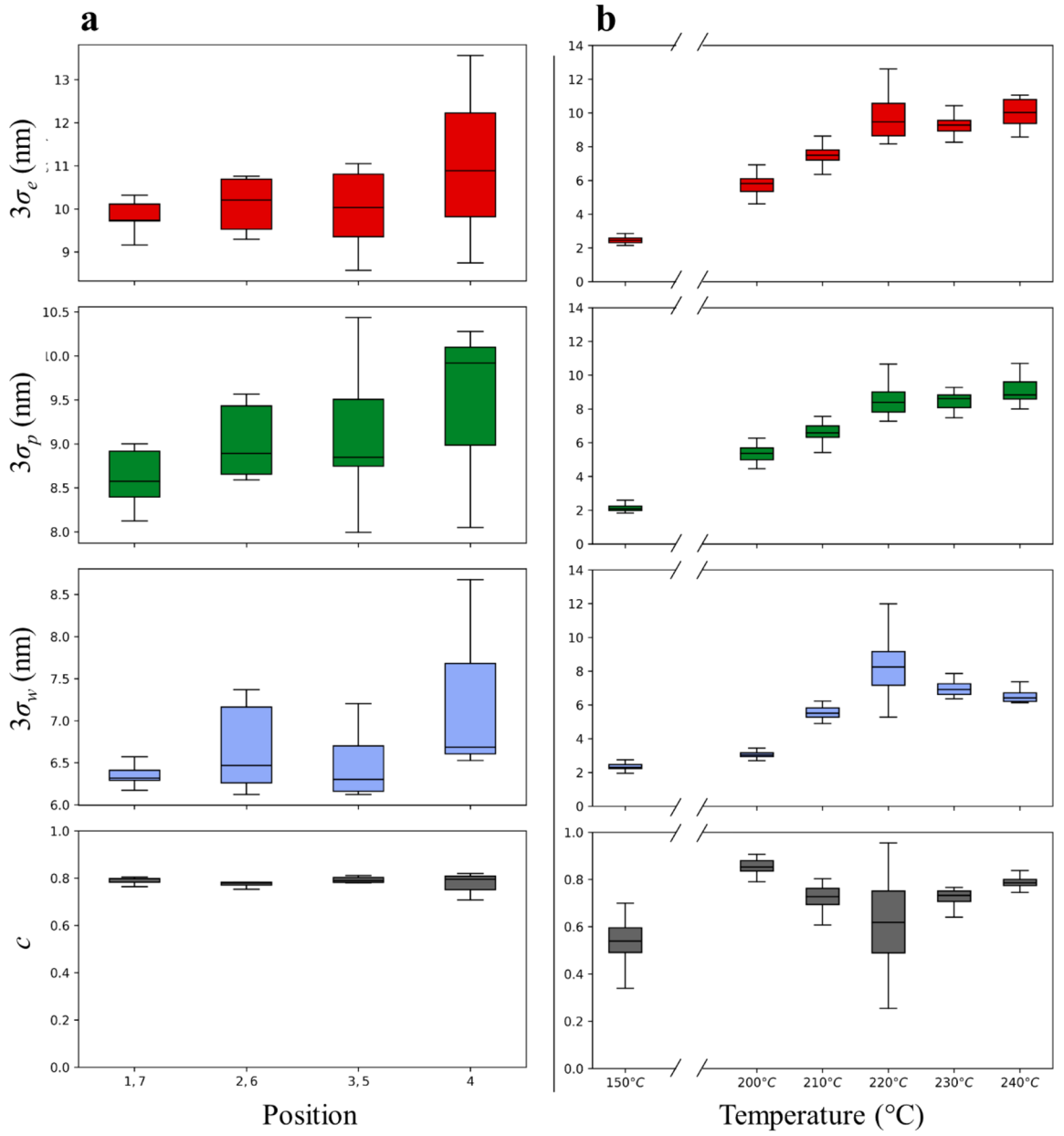

Figure 5. (a) Box plots showing the median and distribution of measured roughness parameters at 240 °C. Roughness varies between cylinders at sidewall positions (i = 1, 7) and those at central positions (i = 4). LER ($3\delta_e$) and LPR ($3\delta_p$), and LWR ($3\delta_w$) are suppressed adjacent to sidewalls, where fluctuations are pinned by the confinement potential. The edge−edge covariance c is constant across the trench. (b) Box plots comparing roughness measurements over *in situ* temperature. Roughness initially increases with temperature and saturates above 220 °C. The value of c increases above 150 °C but varies due to measurement uncertainty. To control for confinement effects, cylinders at sidewall positions (i = 1, 7) are excluded from the temperature series data.

3b−d. Additional examples over varying *in situ* temperature are included in Supporting Information, Figure S3. Roughness parameters based on the variation of each of these terms are categorized as LER, LPR, and LWR. While roughness is conventionally determined from the spatial variation along pattern stripes, here we measure these parameters from the distributions of the time-resolved ensemble. Although we expect spectral dependence to differ in the time domain, the magnitude of fluctuations remains consistent in either ensemble. Following convention, LER is defined as the third standard deviation of the edge position:

$$3\sigma_e = 3\langle \delta e_{i,n}(t)^2 \rangle^{1/2} \tag{4}$$

Similar definitions are used for LPR and LWR:

$$3\sigma_p = 3\langle \delta p_i(t)^2 \rangle^{1/2}; \quad 3\sigma_w = 3\langle \delta w_i(t)^2 \rangle^{1/2} \tag{5}$$

where LPR and LWR are not independent variables, but rather are linked by their definitions in eq 1, and they are related to LER as

$$\sigma_p^{\,2} = \frac{1}{2}\sigma_e^{\,2}(1 + c); \quad \sigma_w^{\,2} = 2\sigma_e^{\,2}(1 - c) \tag{6}$$

where c is the linear correlation coefficient between adjacent edges under the assumption that the edge roughness is consistent across each cylinder. The value of c varies between −1 (total negative correlation), 0 (no correlation), and 1 (total

DOI: 10.1021/acsnano.9b05720
ACS Nano 2019, 13, 11741−11752

positive correlation). Models of the in-phase and out-of-phase behavior of fully correlated and anticorrelated edge fluctuations, respectively, are depicted in Figure 3e,f. We note that in eq 6, positive correlation enhances LPR, while negative correlation enhances LWR. In BCP patterns, polymer chain connectivity and incompressibility lead to coherence between the interfacial positions, and we anticipate positive values for c.[47]

Representative trajectories showing the edge (red points) and placement (green points) fluctuations of a PMMA cylinder for a range of temperatures 150, 210, and 240 °C are shown in Figure 4a. Following thermal equilibration, the observed trajectories remain stable over time throughout SSD imaging. With increasing temperature, fluctuations intensify due to both an increase in thermal energy and a decrease in domain segregation. The resulting trajectories include a set of contributions over frequency space, reflecting a range of dynamic time scales. Each time series tracks a slowly varying low-frequency signal modulated by high-frequency variation. The relative frequency components of each trajectory are described using the discrete power spectral density (PSD) of edge displacements, as shown in Figure 4b. In the plots, the red bands show the first-standard deviation bounds of the PSD signal averaged over 3−10 SSD images, which themselves include multiple trenches and cylinders. Analogous spatial PSD plots of real-space images are frequently used to quantify roughness and correlations in BCP patterns.[28,32] In our temporal PSDs, we observe an increase in roughness at low frequencies, reflecting the combined roughness contribution of multiple polymer chains over longer time scales. With increasing temperature, roughness spectra increase in magnitude and flatten as interaction dynamics extend to higher frequencies.

The PSD plots span a frequency range of 10^{-2} to 10 Hz, limited at low frequency by the survey time and high frequency by the scan rate. Imaging parameters were selected to ensure that the sample region was not influenced by the AFM scanning action, as verified by survey scans following each SSD experiment. Scanning too quickly can lead to abrasion of the polymer surface; scanning for too long can lead to local sample cooling due to the proximity of the AFM tip. Ultimately, these limits define the dynamic regime accessible to our investigation. Because the interdomain fluctuations exceed the rate of our AFM imaging, we see no time correlation in edge positions between line scans. Polymer dynamics faster than the Nyquist frequency cannot be detected and instead contribute to aliasing of the PSD signal, observed as flattening of the PSD at high frequencies.[48,49] More rapid scan rates will be necessary to fully resolve the spectral dependence of interdomain fluctuations.

Although we are unable to resolve time correlations, we do observe significant spatial correlation between cylinder edge displacements at each time step. The measured trajectories show coherence that is not consistent with stochastic thermal noise. To test for the possibility of systemic noise, we considered two controls: (1) comparison of cylinder edges at the same time step in spatially separated trenches and (2) measurements of sidewall motion in substrate trenches without BCP. Under each control condition, we observe no spatial coherence, affirming that our sampling serves as a reliable measure of boundary dynamics. Information on the roughness and correlation of the empty trench sidewalls is reported in Figure S4 in the Supporting Information. Further discussion and analysis of spatial correlations of cylinder fluctuations are expanded on below.

Line Roughness. In the strong-segregation limit, the interdomain boundary has a finite width where the composition continuously transitions between PS and PMMA.[21,50] When examined in systems quenched below T_g, the block composition varies along the boundary resulting in spatial roughness. Above T_g, the interface is dynamic and is continuously modulated by fluctuations as seen above in Figure 4a, and these fluctuations, in turn, contribute to the pattern roughness. Because thermal annealing conditions are difficult to access experimentally, roughness has been traditionally measured in cooled samples. However, our *in situ* measurements allow for analogous determination of roughness parameters in the time domain.

To understand the effect of the confining potential, we consider LER ($3\delta_e$), LPR ($3\delta_p$), and LWR ($3\delta_w$) as a function of domain position. We find that each of the roughness parameters and their associated uncertainties are enhanced with increasing distance from the trench sidewalls at 240 °C, as shown in Figure 5a. The sidewalls act as external guiding fields and suppress interfacial fluctuations of sidewall-adjacent cylinders (i = 1, 7).[31,51] At the center of the trenches, polymer domains are insulated from the hard sidewall by neighboring cylinders and experience a local environment that more closely resembles unconfined polymer, leading to increased roughness. Interestingly, we measure a consistent value of $c \sim 0.78$ at 240 °C, suggesting that the enhanced roughness does not result from changes in interfacial correlation. This finding contrasts with phase-field simulations of confined polymer in which Bosse identified damping of the interface−interface covariance in the proximity of the guiding field.[30] This discrepancy arises because we examined PMMA cylinders, as opposed to the two-dimensional and fully symmetric patterns studied in Bosse's simulations. Cylinders act as incompressible units which have uniformly high interfacial correlation and are therefore less susceptible to the influence of the guide pattern. A complete list of values for $3\delta_e$, $3\delta_p$, $3\delta_w$, and c as a function of trench position are collected in Table 1, with uncertainties corresponding to their first standard deviation.

Table 1. LER, LPR, LWR, and Edge−Edge Covariance As a Function of Position within the Trench[a]

position (at 240 °C)	$3\delta_e$ (nm)	$3\delta_p$ (nm)	$3\delta_w$ (nm)	c
1, 7	9.8 ± 0.4	8.6 ± 0.3	6.4 ± 0.1	0.79 ± 0.01
2, 6	10.5 ± 1.3	9.2 ± 0.7	6.9 ± 0.9	0.78 ± 0.03
3, 5	10.0 ± 0.9	9.1 ± 0.8	6.5 ± 0.4	0.79 ± 0.02
4	11.1 ± 2.0	9.4 ± 1.0	7.3 ± 1.0	0.77 ± 0.05

[a]Uncertainties correspond to the first standard deviation bounds.

In addition to measurements across trenches, our *in situ* imaging allows us to directly measure LER, LPR, and LWR at a series of temperatures above T_g, as plotted in Figure 5b. At 150 °C, we measure a baseline fluctuation intensity consistent with the instrumental response at room temperature, as shown in Figure S3 in the Supporting Information. Above 150 °C, roughness parameters, based on averages from multiple data sets at each temperature, initially increase with temperature due to an enhancement of thermal fluctuations alongside an accompanying decrease in the domain segregation strength. However, above 220 °C, the roughness plateaus, and we find

DOI: 10.1021/acsnano.9b05720
ACS Nano 2019, 13, 11741−11752

limiting values of $3\delta_e \sim 10$ nm, $3\delta_p \sim 9$ nm, and $3\delta_w \sim 7$ nm. In our system, the range of cylinder positions is constrained by the confining trench, which determines an upper limit for LER and LPR. Meanwhile, variations in cylinder widths are limited by the chain length and domain incompressibility, setting an upper bound for LWR.

In all cases, our measurements include contributions from both cylinder fluctuations and AFM imaging noise. However, at 220 °C, imaging noise is further amplified due to reduced phase contrast between the polymer domains. At this temperature, PS and PMMA have similar interaction energetics with the air interface, consequently lowering their contrast during AFM imaging.[52]

Over the temperatures surveyed, we measure positive values for c in the range from $c \sim 0.5$ to 0.9. At 150 °C, where fluctuations are relatively small, dynamics at one interface have a minor influence on neighboring interfaces, and we measure $c = 0.54 \pm 0.10$. Above 150 °C, coherence helps accommodate the strain of increased fluctuations, leading to a general increase in the value of c. However, we see large variation in c at 220 °C that can be partially attributed to imaging noise, resulting in an apparent decorrelation of edge measurements. Mean values for $3\delta_e$, $3\delta_p$, $3\delta_w$, and c as a function of temperature are collected in Table 2, with uncertainties corresponding to their first standard deviation.

Table 2. LER, LPR, LWR, and Edge−Edge Covariance As a Function of Temperature[a]

temperature (°C)	$3\delta_e$ (nm)	$3\delta_p$ (nm)	$3\delta_w$ (nm)	c
150	2.5 ± 0.2	2.1 ± 0.2	2.4 ± 0.2	0.54 ± 0.10
200	5.8 ± 0.5	5.4 ± 0.4	3.1 ± 0.2	0.86 ± 0.03
210	7.7 ± 1.7	6.8 ± 1.2	5.7 ± 1.5	0.72 ± 0.05
220	10.2 ± 2.5	8.6 ± 1.3	8.4 ± 1.7	0.60 ± 0.22
230	9.3 ± 0.6	8.5 ± 0.5	7.0 ± 0.4	0.72 ± 0.04
240	10.3 ± 1.3	9.1 ± 0.8	6.7 ± 0.7	0.78 ± 0.03

[a]Uncertainties correspond to the first standard deviation bounds.

When interpreting these values, we note that AFM imaging is limited to measuring the structure and roughness of the BCP pattern at the atmospheric interface, and we therefore expect our analysis to overestimate roughness. At the free surface, the polymer forms a melt-like layer with increased chain mobility, leading to heightened fluctuations.[53−55]Three-dimensional surveys of BCP interfaces have confirmed that surface roughness is enhanced with respect to the bulk.[33,35]

Spatial Correlation. Within each trench, cylinder motions are coupled. The coherent behavior of the striped pattern may be described by a continuum model in which the motion of spatially separated cylinders is coupled by a set of collective undulatory and peristaltic modes. LPR is directly associated with cylinder undulations, and LWR is similarly associated with peristalsis, but is also influenced by bulk composition fluctuations.[33]

Heretofore, we have only examined the correlations between adjacent interfaces across a PMMA cylinder. We generalize our previous analysis to include long-range correlations using Pearson correlation coefficients (PCC) to identify correlations for a pair of edges $e_{i,n}$ and $e_{j,m}$ at each time step t:

$$\rho_e(i, n; j, m) = \frac{\mathrm{cov}(e_{i,n}(t), e_{j,m}(t))}{\sigma_e(i, n)\sigma_e(j, m)} \quad (7)$$

where $\mathrm{cov}(\cdot)$ measures the covariance and $\sigma_e(i,n)$ is the standard deviation of the n-th edge of the i-th cylinder.[56] This methodology follows a procedure employed by Constantoudis *et al.* to describe cross-line correlations in DSA-templated patterns.[26] Similar definitions may be used to compare cylinder widths and placements. This approach allows us to measure the extent of lateral correlation across a trench based on PCC values ranging from −1 (negative correlation) to 1 (positive correlation). Figure 6 shows a set of correlation matrices comparing the positions of cylinder edges, placements, and widths over a temperature series of 150, 210, and 240 °C. In these plots, each matrix element compares the position of a reference cylinder to that of another cylinder in the trench at the same time step. Correlations are then averaged over time and over multiple trenches to generate PCC matrices representative of the statistical correlation for each pair of cylinders. The matrices are symmetric, and diagonal elements have an autocorrelation of unity. Collectively, these plots reveal trends in fluctuation intensity and correlation as functions of temperature and domain separation.

Correlations of edge fluctuations are shown in Figure 6a. Over this series, we observe that the strength and extent of spatial correlations are enhanced with increasing temperature. At 150 °C, adjacent domains, which are offset by one from the matrix diagonal, show positive correlation, while more separated domains show weaker correlations. Increasing the temperature to 210 °C, we find that the intensity of the positive correlations strengthens and that the range of coherence increases to include most of the trench, while still smoothly decreasing with separation. Finally, at 240 °C robust, positive correlations extend fully across the trench, indicating strong coupling between the confined cylinder edges. This range exceeds correlation lengths measured of DSA patterns on chemically templated substrates, in which correlations are limited by the three-fold periodicity of the underlying guide pattern.[26]

While edge correlations are consistently positive, the intensity of correlations between adjacent cylinders is observed to modulate between alternating edges: Edges that span PMMA domains ($e_{i,L} \rightarrow e_{i,R}$) show a stronger correlation than those across PS domains ($e_{i,R} \rightarrow e_{i+1,L}$). The effect is most apparent when examining the adjacent off-diagonal terms in Figure 6a at 150 °C. With increasing temperature, the intensity difference between alternating matrix elements narrows as the system becomes globally coherent. This contrast arises because the longer-chain PS domains have greater configurational flexibility, and elastic deformation of the majority block more effectively screens interfacial correlations. The PMMA cylinders are comparatively inflexible, leading to a stronger edge correlation. As such, the predominant stable mode of our system is characterized by undulations of the minority-block PMMA cylinders in the PS matrix.[57]

Next, in Figure 6b, we examine correlations between cylinder placements, which are directly related to undulatory oscillatory modes. The motion of placements is positively correlated, that is, as one cylinder oscillates, its neighbors tend to move in the same direction. At 150 °C, we observe weak positive correlation between nearest neighbors, which further weakens between more distant cylinders. Then, at 210 °C, we find a significant increase in the strength of placement correlations that propagate throughout the cylinders in the trench. However, we observe that the coherence of sidewall-adjacent cylinders ($i = 1, 7$) is damped, due to the rigidity of

DOI: 10.1021/acsnano.9b05720
ACS Nano 2019, 13, 11741−11752

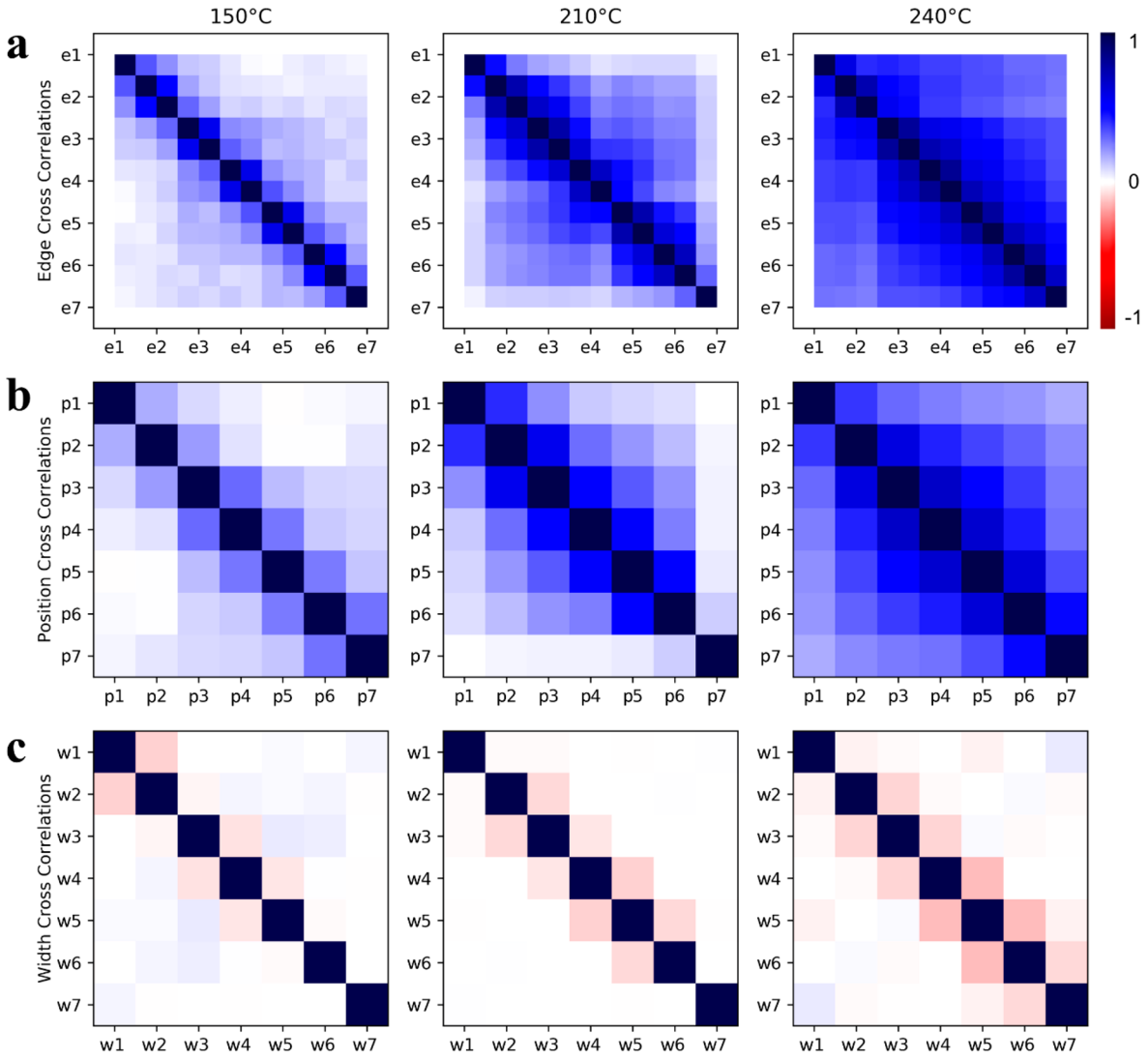

Figure 6. (a) PCC matrices show cross correlations of edge positions across the trench at 150, 210, and 240 °C. Each matrix element is colored according to the PCC value for a pair of edge residuals $\delta e_{i,n}$ and $\delta e_{j,m}$. The matrices are symmetric, and diagonal elements have an autocorrelation of 1. At 150 °C, the edge displacements of adjacent cylinders show positive correlation, and the correlation strength decreases with separation. As the temperature is increased to 210 and 240 °C, the magnitude and range of correlations increase to extend across the trench. The left- and rightmost edges, which were not directly fit, are not included in the matrices. (b) PCC matrices of cylinder placements at 150, 210, and 240 °C. At 150 °C. Positive correlation is observed between the placements of adjacent cylinders, which weakens with greater separation. With increasing temperature, the range and magnitude of placement correlation increase to extend across the trench, which we associate with coherent undulatory modes. (c) PCC matrices of cylinder widths at 150, 210, and 240 °C. Minimal correlation is observed at 150 °C, while at higher temperatures the widths of adjacent cylinders become negatively correlated. The range of the width anticorrelation, which is associated with peristaltic modes, does not extend beyond adjacent cylinders.

the lithographic trench. Finally, we find complete coherence of cylinder placements at 240 °C, with a small decrease along the sidewalls. These correlations arise from in-phase edge dynamics and correspond to a collective undulatory mode. The similar trends between edge and placement correlations are expected because placements are determined from the numerical average of directly adjacent edges, which are observed to be positively correlated in all temperatures surveyed.

Correlations between cylinder widths, shown in a set of PCC plots in Figure 6c, are comparatively weak. At 150 °C, we see minimal correlation between cylinder widths at any separation. With increasing temperature, at 210 °C, we observe anticorrelation between adjacent cylinders with no long-range coupling. Due to coupling of peristaltic modes, extension of one domain induces compression in its neighbors, leading to anticorrelated behavior. The strength of the anticorrelation between adjacent cylinders is further increased at 240 °C, but there is no corresponding increase in range. Global coherence is mitigated by the contribution of local composition fluctuations to width variation.[33] Notably, we observe that the magnitude of the anticorrelation at 210 and 240 °C is suppressed for cylinders i = 1, 7, due to stabilization from the trench sidewalls.[30,47]

Due to the BCP microstructure, interfacial fluctuations are inherently structurally anisotropic. Our SSD measurements, which show long-range coherence extending across multiple domains to encompass the trench, only examine behavior perpendicular to the cylinder alignment. Previous studies have found that small-angle fluctuations in BCP patterns form

DOI: 10.1021/acsnano.9b05720
ACS Nano 2019, 13, 11741−11752

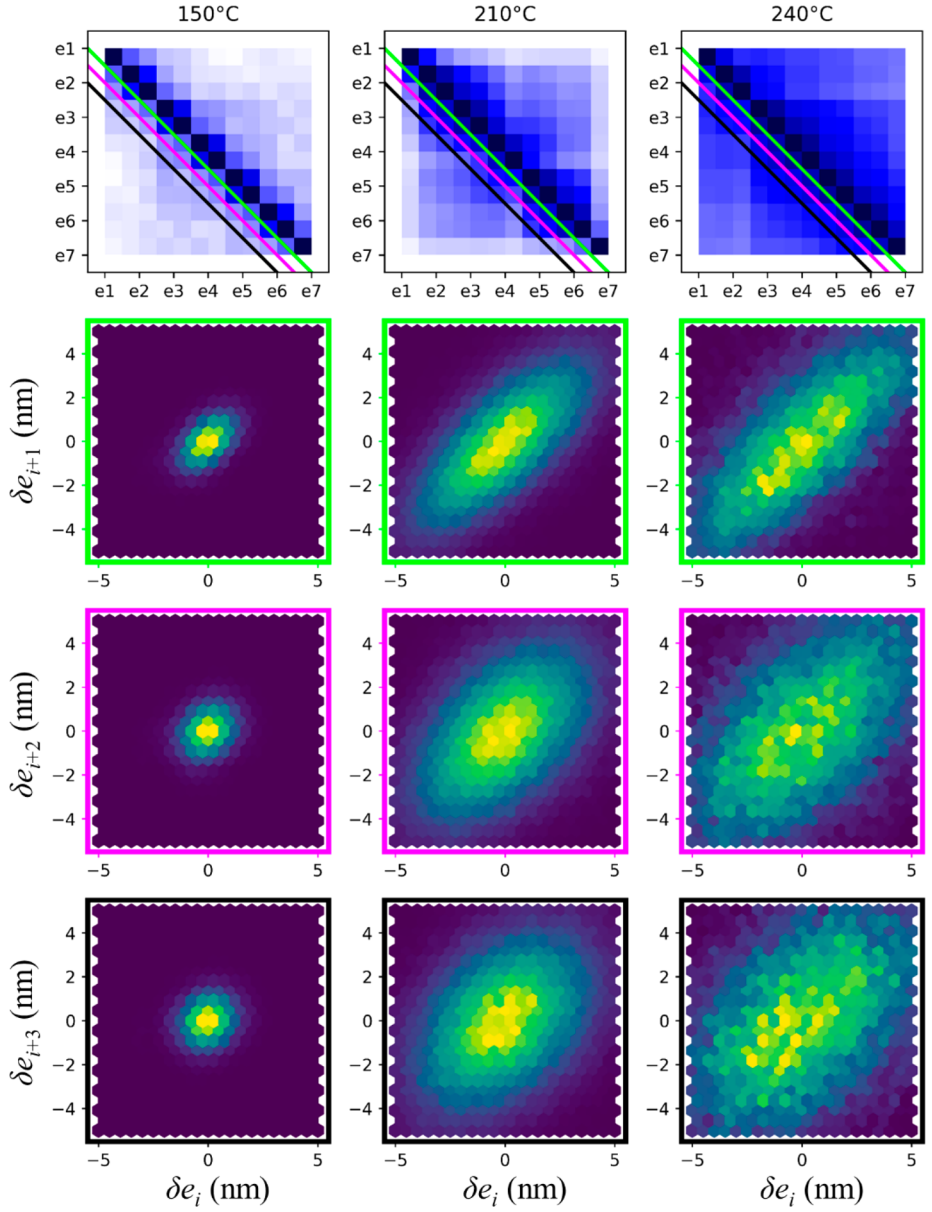

Figure 7. Two-dimensional histograms showing the pairwise distributions of edge displacements over a series of cylinder separations (first, second, and third order) and temperatures (150, 210, and 240 °C). Each plot corresponds to a set of off-diagonal PCC matrix elements as indicated by the colored lines. The distribution spread shows the magnitude of fluctuations, while the distribution shape indicates correlation between the edge displacements. The fluctuation magnitude increases with increasing temperature, and the covariance decreases with increasing separation.

anisotropic grains oriented orthogonally to BCP pattern.[44,58] Although inaccessible to our one-dimensional measurement technique, we expect a shorter length scale for correlations along the axis parallel to the stripes, which have predominant wavelength contributions on the order L_0.

As an additional representation of fluctuation correlation, sets of pairwise distributions of edge displacements are collected in hexagonally binned, two-dimensional histograms, shown in Figure 7, for a series of domain separations (first, second, and third order) and temperatures (150, 210, and 240 °C). Each histogram corresponds to a collection of cylinder pairs with uniform domain separation, as indicated by the colored diagonal lines in the associated PCC matrices. Hexagonal binning allows for visualization of the magnitude and correlation of roughness without biasing toward horizontal and vertical gridlines, while also displaying nearest-neighbor symmetry. From the variance and shape of the distributions, we obtain information on both fluctuation intensity and coherence: Tight clustering signifies small fluctuations, while a wide distribution indicates large fluctuations. As shown in Figure 7, the distribution is initially compact at 150 °C and broadens with increasing temperature as fluctuations are enhanced. Meanwhile, covariance in the pairwise edge displacements, which appears as a linear trend in the histogram plots, directly corresponds to correlations of the associated PCC matrix. At all temperatures, the plots become less linear and more diffuse with increasing separation as edge displacements become decoupled. Generally, we observe that edge fluctuations increase with temperature and become less correlated with increasing domain separation.

DOI: 10.1021/acsnano.9b05720
ACS Nano 2019, 13, 11741−11752

These trends result from local coupling of cylinder dynamics by BCP chain connectivity and compositional constraints. At each time point, the transient structure reflects a thermal perturbation from the equilibrium state, as determined by a balance between the enthalpic penalty of polymer mixing and the entropic freedom of the random coil.[3] Increasing temperature weakens domain segregation, resulting in enhanced composition fluctuations and interfacial broadening.[22] With increased thermal energy, the polymer chains also have greater configurational freedom, which is visible as increased interfacial roughness. The associated interfacial tension and bending strain from edge displacement are accommodated by neighboring domains, leading to correlated motion. At 150 °C, the observed edge perturbations are small, with a range of ∼2 nm, and become sufficiently damped by one neighboring domain. Comparatively, at 240 °C, edge displacements have magnitudes of ∼5 nm, roughly 20% of the cylinder width, resulting in large deviations from their equilibrium positions, and stabilization from correlated motion becomes significant. Our measured displacements correspond closely with interfacial widths of 4.9 ± 0.1 nm reported by Stein *et al.* in lamellar PS-*b*-PMMA after thermal annealing at 240 °C and quenching to room temperature. Fluctuations during thermal annealing directly contribute to the ultimate quenched roughness.[24]

CONCLUSION

Lithographic templating applications of aligned DSA systems rely on careful understanding and control over structural disorder in BCP patterns. While previous investigations have characterized roughness in quenched, room-temperature systems, *in situ* high-speed AFM imaging serves as a direct method for capturing the BCP dynamics above T_g. High-temperature imaging represents a significant step in understanding the intrinsic connection between the assembly of BCP patterns and dynamic fluctuations. Using SSD AFM imaging, we find that roughness scales with the annealing temperature and saturates above 220 °C. We identify robust spatial correlation that extends laterally across each individual confining trench. This coherence reflects continuum behavior in which cylinder oscillations may be described as a set of undulatory and peristaltic modes. These coupled dynamics directly contribute to the roughness and structural disorder of BCP patterns. In the future, we hope to examine time-dependent correlations and believe this to be feasible in higher molecular weight systems. Fluctuations should be understood not just as a barrier to pattern alignment, but as fundamental to thermal annealing and defect healing of BCP thin films.

METHODS

Silicon wafer substrates (purchased from Virginia Semiconductor) were ultrasonically cleaned under toluene, acetone, and isopropanol and dried with N_2. Trench patterns were created by electron-beam lithography using an FEI NanoSEM 230 with PMMA as the electron-beam resist. After developing in methyl isobutyl ketone for 35 s, the patterned samples were rinsed with isopropanol and dried with N_2. Patterns were transferred to the silicon wafers with CF_4 and O_2 plasma dry etching, using a South Bay Technologies, Inc. RIE-2000. The resulting trenches were about 375 nm wide and 50 nm deep.

Cylinder-forming PS-*b*-PMMA (55−22k, PDI 1.09) with L_0 = 44.1 ± 1.7 nm was purchased from Polymer Source. A 0.9 wt % polymer solution was prepared in toluene and spin coated at 3000 rpm for 50 s onto the patterned substrates to produce a monolayer within the trench patterns. Global film thicknesses were measured with a Gaertner Waferskan ellipsometer and found to be roughly 20 nm.

After pre-annealing in a tube furnace under argon at 250 °C for 8 h to produce aligned patterns (*i.e.*, locally free of defects), samples were imaged with an Asylum Cypher ES Environmental AFM. A single sample was stepped over a series of *in situ* temperatures from 150 to 240 °C while under argon flow with cell gauge pressures of 30−40 mbar. The sample was initially heated to 150 °C at a ramp rate of 2 °C/s and was then subsequently ramped through each experimental temperature without returning to room temperature. The sample equilibrated for at least 5 min at each temperature before imaging; equilibration was verified by comparing results over a sequence of images over time.

High-speed, tapping-mode imaging was performed using gold-coated Arrow UHF cantilevers with resonant frequency of 1−1.5 MHz, achieving a scanning rate of 20 Hz and 5.9 nm pixel resolution. For our measurements, the slow-scan axis was disabled, yielding an effective time resolution of 50 ms per line. Images were collected with a 500 mV set point and in repulsive mode. These scanning parameters were selected to reliably track surface features while avoiding sample degradation. Following each measurement, the surrounding sample region was inspected to verify that the pattern was not locally damaged by the AFM scan.

Subpixel edge tracking is achieved through linear interpolation of the AFM data. A large pixel size was necessary (1) to include multiple trenches in each image and (2) to prevent sample damage. Including multiple trenches in each image allowed us to confirm that only cylinders in the same trench were correlated to each other and that the correlations were not an artifact of the AFM line scan. Imaging over a large region also distributed AFM interaction forces over a larger scan area.

All images were collected from the same region of one sample to control for any variations in polymer film thickness or in the lithographic trench boundaries. Throughout the imaging process, the local film thickness over patterned regions remained consistent, as confirmed from AFM topography images. Pattern pitch was found to be constant within error over the temperature range surveyed, as shown in Supporting Information, Figure S3. Drift was minimal, less than 80 pm across the measurement time of a single image. Drift correction produced no deviation in the resulting PSD plots, as discussed in the Supporting Information, Figure S5.

To accurately and reproducibly track and analyze domains, we used a custom image analysis software written in Python based on the SciPy framework.[59] At each temperature, the approximate location of the first PMMA domain in each trench was manually located on the time-averaged phase trace; the six successive PMMA domains were then identified by finding the next six local minima. Each phase trace was then processed in parallel to find the true position of each domain at a given time step. In this procedure, the approximate cylinder placement was updated to the nearest local phase minimum. The neighboring left and right maxima then defined a local window that encompassed the interfaces between a given PMMA domain and its two adjacent PS domains. The first derivative of the phase signal was then fit with a model Gaussian to precisely locate the extrema positions, corresponding to the steepest slope of the phase and, thus, the PS/PMMA domain edges. An example of this procedure is illustrated in Figure 2 and the Gaussian fitting process is further discussed in the Supporting Information, Figure S1. The phase signal was not well-defined at the boundary of the trenches due to a rapidly changing sample topography. To account for this, the leftmost and rightmost edges along the trench were determined by doubling the distance between the first-derivative maximum and half-maxima. For each of these experiments, we analyzed data sets ranging from 3 to 10 images. Altogether, at 150 °C, we averaged over a total of 129,024 points for widths and placements (doubled for edges), 86,368 points at 210 °C, and 28,672 points at 240 °C.

DOI: 10.1021/acsnano.9b05720
ACS Nano 2019, 13, 11741−11752

ASSOCIATED CONTENT

Supporting Information

The Supporting Information is available free of charge on the ACS Publications website at DOI: 10.1021/acsnano.9b05720.

Figures S1−S5 contain the following: Gaussian modeling of the phase data; pattern pitch over temperature; histograms of roughness parameters over temperature; roughness measurements of trenches without confined BCP; and analysis of our drift correction procedure (PDF)

AUTHOR INFORMATION

Corresponding Author

*E-mail: s-sibener@uchicago.edu.

ORCID

S. J. Sibener: 0000-0002-5298-5484

Notes

The authors declare no competing financial interest.

ACKNOWLEDGMENTS

This work was supported by the U.S. Department of Commerce, National Institute of Standards and Technology, under award no. 70NANB19H005 as part of the Center for Hierarchical Materials Design. This was also supported by the NSF-Materials Research Science and Engineering Center at The University of Chicago, grant no. NSF-DMR-14-20709.

REFERENCES

(1) Darling, S. B. Directing the Self-Assembly of Block Copolymers. *Prog. Polym. Sci.* **2007**, *32*, 1152−1204.

(2) Bates, C. M.; Maher, M. J.; Janes, D. W.; Ellison, C. J.; Willson, C. G. Block Copolymer Lithography. *Macromolecules* **2014**, *47*, 2−12.

(3) Fredrickson, G. H.; Bates, F. S. Dynamics of Block Copolymers: Theory and Experiment. *Annu. Rev. Mater. Sci.* **1996**, *26*, 501−550.

(4) Bates, C. M.; Bates, F. S. 50th Anniversary Perspective: Block Polymers—Pure Potential. *Macromolecules* **2017**, *50*, 3−22.

(5) Liu, C.; Ramírez-Hernández, A.; Han, E.; Craig, G. S. W.; Tada, Y.; Yoshida, H.; Kang, H.; Ji, S.; Gopalan, P.; de Pablo, J. J.; Nealey, P. F. Chemical Patterns for Directed Self-Assembly of Lamellae-Forming Block Copolymers with Density Multiplication Features. *Macromolecules* **2013**, *46*, 1415−1424.

(6) Ruiz, R.; Kang, H.; Detcheverry, F. A.; Dobisz, E.; Kercher, D. S.; Albrecht, T. R.; de Pablo, J. J.; Nealey, P. F. Density Multiplication and Improved Lithography by Directed Block Copolymer Assembly. *Science* **2008**, *321*, 936−939.

(7) Sundrani, D.; Darling, S. B.; Sibener, S. J. Guiding Polymers to Perfection: Macroscopic Alignment of Nanoscale Domain. *Nano Lett.* **2004**, *4*, 273−276.

(8) Sundrani, D.; Darling, S. B.; Sibener, S. J. Hierarchical Assembly and Compliance of Aligned Nanoscale Polymer Cylinders in Confinement. *Langmuir* **2004**, *20*, 5091−5099.

(9) Cheng, J. Y.; Ross, C. A.; Thomas, E. L.; Smith, H. I.; Vancso, G. J. Templated Self-Assembly of Block Copolymers: Effect of Substrate Topography. *Adv. Mater.* **2003**, *15*, 1599−1602.

(10) Ryu, H. J.; Tong, Q.; Sibener, S. J. Time-Resolved Analysis of Domain Growth and Alignment of Cylinder-Forming Block Copolymers Confined within Nanopatterned Substrates. *J. Phys. Chem. Lett.* **2013**, *4*, 2890−2895.

(11) Li, W.; Müller, M. Directed Self-Assembly of Block Copolymers by Chemical or Topographical Guiding Patterns: Optimizing Molecular Architecture, Thin-Film Properties, and Kinetics. *Prog. Polym. Sci.* **2016**, *54*−*55*, 47−75.

(12) Garner, G. P.; Rincon Delgadillo, P.; Gronheid, R.; Nealey, P. F.; de Pablo, J. J. Design of Surface Patterns with Optimized Thermodynamic Driving Forces for the Directed Self-Assembly of Block Copolymers in Lithographic Applications. *Mol. Syst. Des. Eng.* **2017**, *2*, 567−580.

(13) Tong, Q.; Zheng, Q.; Sibener, S. J. Alignment and Structural Evolution of Cylinder-Forming Diblock Copolymer Thin Films in Patterned Tapered-Width Nanochannels. *Macromolecules* **2014**, *47*, 4236−4242.

(14) Li, W.; Müller, M. Thermodynamics and Kinetics of Defect Motion and Annihilation in the Self-Assembly of Lamellar Diblock Copolymers. *Macromolecules* **2016**, *49*, 6126−6138.

(15) Hur, S.-M.; Thapar, V.; Ramírez-Hernández, A.; Khaira, G.; Segal-Peretz, T.; Rincon-Delgadillo, P. A.; Li, W.; Müller, M.; Nealey, P. F.; de Pablo, J. J. Molecular Pathways for Defect Annihilation in Directed Self-Assembly. *Proc. Natl. Acad. Sci. U. S. A.* **2015**, *112*, 14144−14149.

(16) Liu, C.-C.; Thode, C. J.; Rincon Delgadillo, P. A.; Craig, G. S. W.; Nealey, P. F.; Gronheid, R. Towards an All-Track 300 mm Process for Directed Self-Assembly. *J. Vac. Sci. Technol., B: Nanotechnol. Microelectron.: Mater., Process., Meas., Phenom.* **2011**, *29*, 06F203.

(17) Stoykovich, M. P.; Daoulas, K. C.; Müller, M.; Kang, H.; de Pablo, J. J.; Nealey, P. F. Remediation of Line Edge Roughness in Chemical Nanopatterns by the Directed Assembly of Overlying Block Copolymer Films. *Macromolecules* **2010**, *43*, 2334−2342.

(18) Patrone, P. N.; Gallatin, G. M. Modeling Line Edge Roughness in Templated, Lamellar Block Copolymer Systems. *Macromolecules* **2012**, *45*, 9507−9516.

(19) Suh, H. S.; Chen, X.; Rincon-Delgadillo, P. A.; Jiang, Z.; Strzalka, J.; Wang, J.; Chen, W.; Gronheid, R.; de Pablo, J. J.; Ferrier, N.; Doxastakis, M.; Nealey, P. F. Characterization of the Shape and Line-Edge Roughness of Polymer Gratings with Grazing Incidence Small-Angle X-Ray Scattering and Atomic Force Microscopy. *J. Appl. Crystallogr.* **2016**, *49*, 823−834.

(20) Witten, T. A.; Leibler, L.; Pincus, P. A. Stress Relaxation in the Lamellar Copolymer Mesophase. *Macromolecules* **1990**, *23*, 824−829.

(21) Semenov, A. N. Theory of Block-Copolymer Interfaces in the Strong Segregation Limit. *Macromolecules* **1993**, *26*, 6617−6621.

(22) Semenov, A. N. Scattering of Statistical Structure of Polymer/Polymer Interfaces. *Macromolecules* **1994**, *27*, 2732−2735.

(23) Srinivas, G.; Swope, W. C.; Pitera, J. W. Interfacial Fluctuations of Block Copolymers: A Coarse-Grain Molecular Dynamics Simulation Study. *J. Phys. Chem. B* **2007**, *111*, 13734−13742.

(24) Stein, G. E.; Liddle, J. A.; Aquila, A. L.; Gullikson, E. M. Measuring the Structure of Epitaxially Assembled Block Copolymer Domains with Soft X-Ray Diffraction. *Macromolecules* **2010**, *43*, 433−441.

(25) Wang, C.; Stein, G. E.; Bosse, A. W.; Wu, W.; et al. Line Edge Roughness of Directed Self-Assembly PS-PMMA Block Copolymers — A Candidate for Future Lithography. *AIP Conf. Proc.* **2011**, *1395*, 305−308.

(26) Constantoudis, V.; Papavieros, G.; Gogolides, E.; Pret, A. V.; Pathangi, H.; Gronheid, R. Challenges in Line Edge Roughness Metrology in Directed Self-Assembly Lithography: Placement Errors and Cross-Line Correlations. *J. Micro/Nanolithogr., MEMS, MOEMS* **2017**, *16*, 024001.

(27) Cutler, C.; Thackeray, J. W.; DeSisto, J.; Nelson, J.; Lee, C.-B.; Li, M.; Aqad, E.; Hou, X.; Marangoni, T.; Kaitz, J.; Rena, R.; Mack, C. A. Roughness Power Spectral Density as a Function of Resist Parameters and Its Impact Through Process. *Proc. of SPIE* **2018**, *10587*, 1058707.

(28) Mack, C. A. Reducing Roughness in Extreme Ultraviolet Lithography. *J. Micro/Nanolithogr., MEMS, MOEMS* **2018**, *17*, 041006.

(29) Bosse, A. W. Phase-Field Simulation of Long-Wavelength Line Edge Roughness in Diblock Copolymer Resists. *Macromol. Theory Simul.* **2010**, *19*, 399−406.

(30) Bosse, A. W. Effects of Segregation Strength and an External Field on the Thermal Line Edge and Line Width Roughness Spectra of a Diblock Copolymer Resist. *J. Vac. Sci. Technol., B: Nanotechnol. Microelectron.: Mater., Process., Meas., Phenom.* **2011**, *29*, 031803.

DOI: 10.1021/acsnano.9b05720
ACS Nano 2019, 13, 11741−11752

(31) Bosse, A. Modeling the Power Spectrum of Thermal Line Edge Roughness in a Lamellar Diblock Copolymer Mesophase. *J. Vac. Sci. Technol., B: Nanotechnol. Microelectron.: Mater., Process., Meas., Phenom.* **2011**, *29*, 06F202.
(32) Ruiz, R.; Wan, L.; Lopez, R.; Albrecht, T. R. Line Roughness in Lamellae-Forming Block Copolymer Films. *Macromolecules* **2017**, *50*, 1037−1046.
(33) Sunday, D. F.; Hammond, M. R.; Wang, C.; Wu, W.-l.; Delongchamp, D. M.; Tjio, M.; Cheng, J. Y.; Pitera, J. W.; Kline, R. J. Determination of the Internal Morphology of Nanostructures Patterned by Directed Self Assembly. *ACS Nano* **2014**, *8*, 8426−8437.
(34) Sunday, D. F.; Ren, J.; Liman, C. D.; Williamson, L. D.; Gronheid, R.; Nealey, P. F.; Kline, R. J. Characterizing Patterned Block Copolymer Thin Films with Soft X-Rays. *ACS Appl. Mater. Interfaces* **2017**, *9*, 31325−31334.
(35) Segal-Peretz, T.; Ren, J.; Xiong, S.; Khaira, G.; Bowen, A.; Ocola, L. E.; Divan, R.; Doxastakis, M.; Ferrier, N. J.; de Pablo, J.; Nealey, P. F. Quantitative Three-Dimensional Characterization of Block Copolymer Directed Self-Assembly on Combined Chemical and Topographical Prepatterned Templates. *ACS Nano* **2017**, *11*, 1307−1319.
(36) Harrison, C.; Adamson, D. H.; Cheng, Z.; Sebastian, J. M.; Sethuraman, S.; Huse, D. A.; Register, R. A.; Chaikin, P. M. Mechanisms of Ordering in Striped Patterns. *Science* **2000**, *290*, 1558−1560.
(37) Hahm, J.; Lopes, W. A.; Jaeger, H. M.; Sibener, S. J. Defect Evolution in Ultrathin Films of Polystyrene-Block-Polymethylmethacrylate Diblock Copolymers Observed by Atomic Force Microscopy. *J. Chem. Phys.* **1998**, *109*, 10111−10114.
(38) Raybin, J.; Ren, J.; Chen, X.; Gronheid, R.; Nealey, P. F.; Sibener, S. J. Real-Time Atomic Force Microscopy Imaging of Block Copolymer Directed Self Assembly. *Nano Lett.* **2017**, *17*, 7717−7723.
(39) Tsarkova, L.; Knoll, A.; Magerle, R. Rapid Transitions between Defect Configurations in a Block Copolymer Melt. *Nano Lett.* **2006**, *6*, 1574−1577.
(40) Tsarkova, L.; Horvat, A.; Krausch, G.; Zvelindovsky, A. V.; Sevink, G. J. A.; Magerle, R. Defect Evolution in Block Copolymer Thin Films *via* Temporal Phase Transitions. *Langmuir* **2006**, *22*, 8089−8095.
(41) Yufa, N. A.; Li, J.; Sibener, S. J. *InSitu* High-Temperature Studies of Diblock Copolymer Structural Evolution. *Macromolecules* **2009**, *42*, 2667−2671.
(42) Hansma, P. K.; Schitter, G.; Fantner, G. E.; Prater, C. High-Speed Atomic Force Microscopy. *Science* **2006**, *314*, 601−602.
(43) Riesch, C.; Radons, G.; Magerle, R. Aging of Orientation Fluctuations in Stripe Phases. *Phys. Rev. E* **2014**, *90*, 052101.
(44) Riesch, C.; Radons, G.; Magerle, R. Scaling Properties of Ageing Orientation Fluctuations in Stripe Phases. *Interface Focus* **2017**, *7*, 20160146.
(45) Sunday, D. F.; Maher, M. J.; Hannon, A. F.; Liman, C. D.; Tein, S.; Blachut, G.; Asano, Y.; Ellison, C. J.; Willson, C. G.; Kline, R. J. Characterizing the Interface Scaling of High χ Block Copolymers near the Order-Disorder Transition. *Macromolecules* **2018**, *51*, 173−180.
(46) Cleveland, J. P.; Anczykowski, B.; Schmid, A. E.; Elings, V. B. Energy Dissipation in Tapping-Mode Atomic Force Microscopy. *Appl. Phys. Lett.* **1998**, *72*, 2613−2615.
(47) Bosse, A. W.; Lin, E. K.; Jones, R. L.; Karim, A. Interfacial Fluctuations in an Ideal Block Copolymer Resist. *Soft Matter* **2009**, *5*, 4266−4271.
(48) Mack, C. A. Systematic Errors in the Measurement of Power Spectral Density. *J. Micro/Nanolithogr., MEMS, MOEMS* **2013**, *12*, 033016.
(49) Mack, C. A. More Systematic Errors in the Measurement of Power Spectral Density. *J. Micro/Nanolithogr., MEMS, MOEMS* **2015**, *14*, 033502.
(50) Shull, K. R.; Mayes, A. M.; Russell, T. P. Segment Distributions in Lamellar Diblock Copolymers. *Macromolecules* **1993**, *26*, 3929−3936.
(51) Geisinger, T.; Müller, M.; Binder, K. Symmetric Diblock Copolymers in Thin Films. II. Comparison of Profiles between Self-Consistent Field Calculations and Monte Carlo Simulations. *J. Chem. Phys.* **1999**, *111*, 5251−5258.
(52) Mansky, P.; Russell, T. P.; Hawker, C. J.; Mays, J.; Cook, D. C.; Satija, S. K. Interfacial Segregation in Disordered Block Copolymers: Effect of Tunable Surface Potentials. *Phys. Rev. Lett.* **1997**, *79*, 237−240.
(53) Keddie, J. L; Jones, R. A. L; Cory, R. A Size-Dependent Depression of the Glass Transition Temperature in Polymer Films. *Europhys. Lett.* **1994**, *27*, 59−64.
(54) Fakhraai, Z.; Forrest, J. A. Probing Slow Dynamics in Supported Thin Polymer Films. *Phys. Rev. Lett.* **2005**, *95*, 025701.
(55) Zhang, Y.; Potter, R.; Zhang, W.; Fakhraai, Z. Using Tobacco Mosaic Virus to Probe Enhanced Surface Diffusion of Molecular Glasses. *Soft Matter* **2016**, *12*, 9115−9120.
(56) Pearson, K. Note on Regression and Inheritance in the Case of Two Parents. *Proc. R. Soc. London* **1895**, *58*, 240−242.
(57) Yeung, C.; Shi, A.-C.; Noolandi, J.; Desai, R. C. Anisotropic Fluctuations in Ordered Copolymer Phases. *Macromol. Theory Simul.* **1996**, *5*, 291−298.
(58) Hammond, M. R.; Kramer, E. J. Edge Effects on Thermal Disorder in Laterally Confined Diblock Copolymer Cylinder Monolayers. *Macromolecules* **2006**, *39*, 1538−1544.
(59) Jones, E.; Oliphant, E.; Peterson, P. et al. SciPy: Open Source Scientific Tools for Python, 2001. http://www.scipy.org/ (accessed February 13, 2018).

DOI: 10.1021/acsnano.9b05720
ACS Nano 2019, 13, 11741−11752